Effect of Solvent Environment on Colloidal-Quantum-Dot Solar-Cell Manufacturability and Performance

*Ahmad R. Kirmani, Graham H. Carey, Maged Abdelsamie, Buyi Yan, Dongkyu Cha, Lisa R. Rollny, Xiaoyu Cui, Edward H. Sargent, and Aram Amassian**

Interest in the field of colloidal quantum dot (QD) photovoltaics has surged over the past decade, prompted by the observation that short conjugated ligands between semiconducting nanocrystals (NCs) can increase the carrier mobility in NC thin films by several orders of magnitude.[1] Amongst semiconducting QDs, lead chalcogenides have attracted the most attention due to their strong light absorption coupled with large Bohr radii (a few tens of nanometers) which assists charge delocalization and leads to higher carrier mobilities.[2–4] Talapin and Murray reported high electron and hole field-effect mobilities (0.9 and 0.2 $cm^2\ V^{-1}\ s^{-1}$ respectively) of initially poorly conducting films of PbSe NCs upon chemical treatment with hydrazine.[5] Conductive PbSe NC-based thin films made by layer-by-layer (LbL) dip-coating and subsequent solid-state ligand exchange were first demonstrated using 1,2-ethanedithiol as the cross-linker, thereby effectively reducing the interparticle distance and enhancing carrier transport.[6]

Following the first demonstration of a solution-processed lead sulphide (PbS) CQD-based solar cell in 2005, power conversion efficiencies (PCEs) as high as 8.5% have since been reported.[7,8] Photon absorption in depleted heterojunction solar cells takes place in a ca. 300 nm thick QD active layer which is constructed in sequential LbL steps (typically ca. 9–12 steps) involving the repetitive deposition of an oleic acid (OA)-capped QD layer, followed by solid-state ligand exchange and solvent wash at each step. The solid-state ligand-exchange process replaces the OA molecules capping the QDs with bifunctional molecules of 3-mercaptopropionic acid (MPA) delivered in a methanol (MeOH) solution. The exchange brings the dots closer for better charge transport, significantly increasing their packing density, and renders the QDs insoluble, which paves the way for the next layer to be deposited.[9] A literature survey reveals that all the high performing PbS-QD-based solar cells reported so far have relied on the LbL deposition process for constructing the absorbing layer.[8,10–12] However, the current LbL process is tedious, extremely wasteful and generally incompatible with scalable solution processing methods which can be applied in a roll-to-roll manner. A solution-phase ligand-exchange strategy was recently reported that allowed a single-step deposition of the QD absorber layer thereby avoiding material waste.[13] However, device performance was found to still be limited by the reduced ligand coverage that resulted in a high density of charge carrier traps, and performance was therefore significantly lower than state-of-the-art devices prepared by the LbL method. We have taken the view that significant improvements are still possible in the LbL process which may lead to the successful implementation of a single step QD thin film followed by ligand exchange, with the important requirement of maintaining benchmark solar-cell performance.

The absence of any studies reporting efficient solar cells fabricated in much less than 10 steps highlights possible limitations of the current LbL scheme. To illustrate the problem, we have fabricated a state-of-the-art device with ca. 7% power conversion efficiency (PCE), made with a 300 nm absorbing layer fabricated in 80 nm/30 nm (pristine/exchanged) steps including a three-second-long ligand exchange (see **Figure 1** for J–V characteristics and **Table 1** for device characteristics). We then fabricated a similar device with a reduced number of steps (3 instead of 10), effectively building up the absorbing layer in ca. 250 nm/100 nm steps, but without extending the ligand-exchange duration; not surprisingly, we observed a significant performance loss (down to ca. 5% PCE), likely due to incomplete ligand exchange within the thicker QD films, as evidenced by low J_{sc}. We therefore extend the ligand exchange and find, to our surprise, the devices perform even worse (ca. 3.7% PCE), due in large part to a reduction in V_{oc}, indicative of trap formation. It should be noted that the limitation to three layers was dictated by the fact that spin-coating could not achieve QD films thicker than 250 nm/100 nm (pristine/exchanged).

We take the view that extended solvent–QD interactions during the ligand-exchange step may be the culprit of the device performance degradation. Our evaluation of solvent effects reported in this communication reveals indeed that MeOH, the ligand-exchange solvent, chemically damages the QDs by leaching the chlorine (Cl) atomic passivant when the ligand exchange is extended beyond a few seconds. Next, we

A. R. Kirmani, M. Abdelsamie, B. Yan, Dr. D. Cha, Prof. A. Amassian
Division of Physical Sciences and Engineering
Solar and Photovoltaic Engineering Research Center (SPERC)
King Abdullah University of Science and Technology (KAUST)
Thuwal 23955–6900, Saudi Arabia
E-mail: aram.amassian@kaust.edu.sa
G. H. Carey, L. R. Rollny, Prof. E. H. Sargent
Department of Electrical and Computer Engineering
University of Toronto
Toronto, Ontario M5S 3G4, Canada
Dr. X. Y. Cui
Canadian Light Source
Saskatoon, SK S7N 2V3, Canada

DOI: 10.1002/adma.201400577

ADVANCED MATERIALS
www.advmat.de

www.MaterialsViews.com

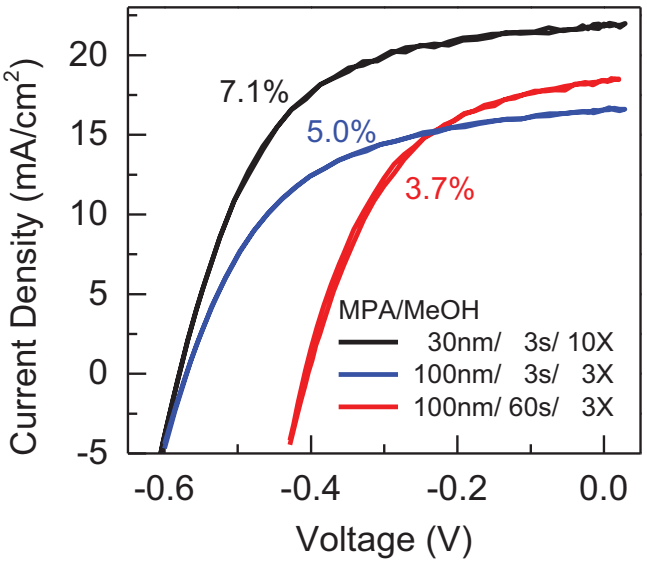

Figure 1. Typical current–voltage profiles for a standard processed device – a solid-state exchange using 3-mercaptopropionic acid (MPA) in methanol, treated for 3 s per 30 nm layer (black) and reduced material devices, treated for 3 s per 100 nm layer (blue) and for 60 s per 100 nm layer (red).

demonstrate this chemical damage can be avoided entirely by using an aprotic and high-dipole-moment organic solvent, such as acetonitrile (ACN), which leaves the QDs physically and chemically intact even after extended exposure. Using ACN, we successfully demonstrate a state-of-the-art QD solar cell employing an active layer fabricated in only 3 steps. The new insight into the role of the solvent in the ligand-exchange process is expected to lead to single step preparation of QD absorber, paving the way for large area roll-to-roll manufacturing of efficient CQD solar cells.

It has been long known that the carboxylic hydrogen atom plays a decisive role in the solubility of oleic acid.[14] In hydroxyl group-containing solvents such as MeOH the carboxylic hydrogen of OA can compete with the internal hydrogen bonding in the solvent giving rise to high solubility of OA in MeOH. For nitrogen-containing solvents such as ACN, wherein the intermolecular dipole moments are very high, the carboxylic hydrogen of OA is unable to form hydrogen bonds with the solvent and hence OA is poorly soluble. Both MeOH and ACN dissolve the MPA ligand effectively and thus allow us to focus the first part of our investigation on solvent-QD interactions. A key difference in the solvent-QD interactions is illustrated in **Figure 2**a,b, where we have compared Fourier transform infrared (FTIR) transmittance spectra of a pristine QD film with that of a film exposed to MeOH and ACN for 10 min. The spectra reveal significant loss of oleic acid from the QD surface upon extended interaction with MeOH. Atomic ratio of OA to lead for the pristine and solvent treated films as measured from XPS are shown in the insets of Figure 2a,b. MeOH treatment results into a decrease of the capping OA content, whereas ACN treatment seems benign in comparison. It should however be noted that since the carbon signal in XPS includes the adventitious surface carbon footprint, the C:Pb ratio should be considered to be depicting only a qualitative rather than a quantitative trend.

Table 1. Device properties for CQD thin films processed according to three different recipes. A solid-state exchange using 3-mercaptopropionic acid (MPA) in methanol, treated for 3 s per 30 nm layer for a total of 10 layers, 3 s per 100 nm layer for a total of 3 layers, and 60 s per 100 nm layer for a total of 3 layers.

	V_{OC} [V]	J_{SC} [mA/cm^2]	FF [%]	PCE [%]
MeOH – 3 s/30 nm	–0.580	21.5	56.7	7.07
MeOH – 3 s/100 nm	–0.572	16.4	52.8	4.99
MeOH – 60 s/100 nm	–0.409	18.1	49.6	3.67

We have probed the interaction of the MeOH and ACN solvents with QDs in detail using a quartz crystal microbalance with dissipation (QCM-D) capability. QCM-D measures the mass loading/unloading on the surface of an AT-cut quartz sensor in terms of a shift in its resonance frequency.[15–17] Due to the strong impedance mismatch between the quartz crystal and the solution medium, only a shallow evanescent wave propagates into the solution, making the QCM-D technique only sensitive to the addition or loss of mechanically bound mass. It is also insensitive to evaporative loss of solvent from the bulk solution for the same reason. As such, it should be sensitive to OA removal as well as to the loss or not of QDs when solvent-treated QDs are exposed to octane, a good solvent for CQDs. QCM-D reveals significant mass loss upon dropping MeOH onto a QD-coated QCM-D crystal, indicating exponential decay of mass (Figure 2c). The mass loss detected by QCM-D suggests the detachment of OA from the QD surface and its subsequent dissolution into the solution above the sensor. The process appears to stabilize within 200 s, with most of the mass loss observed in the initial 100 s of MeOH exposure, whereas no noticeable change is detected in case of ACN-treated QD films. Following a 100 s exposure to MeOH or ACN, octane was dropped upon the surface of the N_2-dried QD film. The ACN-treated QDs dissolved nearly completely (Figure 2d) in a matter of seconds, whereas the MeOH-treated QDs remained immobilized on the surface. Infrared variable-angle spectroscopic ellipsometry (IR-VASE) measurements were performed in reflection mode on QD films (see Figure S1, Supporting Information) to probe the extent of OA loss with solvent exposure time. The IR signature of the C–H stretching vibrations in OA at 2852 cm^{-1} and 2922 cm^{-1} were followed over successive solvent treatments to track the evolution of OA content.[10] Over a period of 10 min, MeOH removes approximately 80% of the OA whereas ACN shows only a 10% decrease (Figure 2e). IR-VASE measurements reveal the time-evolution of OA content in the QD films and indicate that 40% overall loss of OA is required to render the QD film entirely insoluble in octane. During this period, the MeOH-treated film collapses to ca. 60% of its initial thickness accompanied by densification, as suggested by significant increase of the refractive index as per UV–vis–NIR VASE measurements (Figure S2, Supporting Information). When treated for shorter times, MeOH is believed to remove OA predominantly from QDs near the top surface of the film, which renders parts of the film insoluble in octane with the OA-rich QDs still breaking through the crust and dissolving in

DOI: 10.1002/adma.201400577

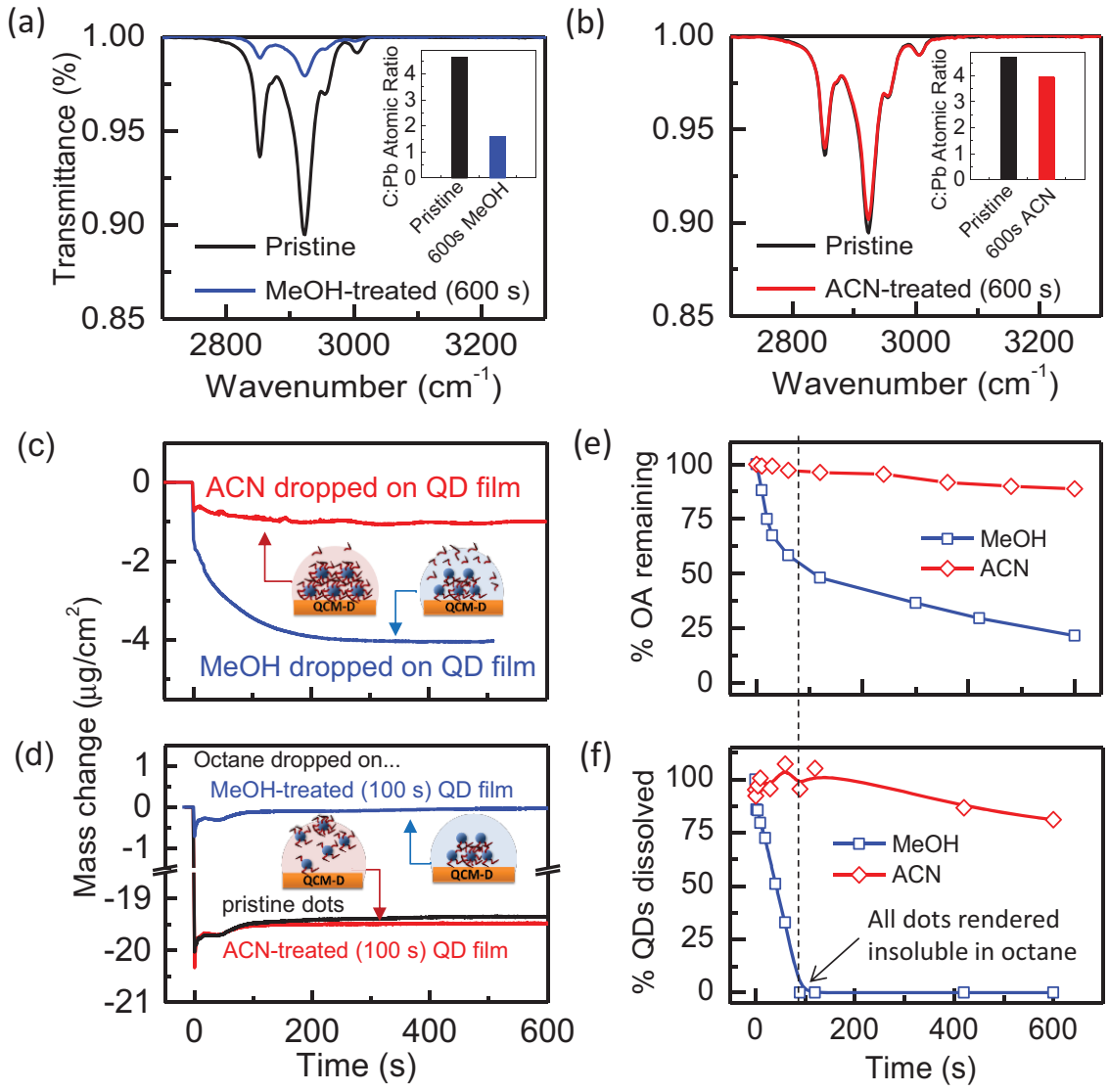

Figure 2. Fourier transform infrared (FTIR) spectra showing the C–H stretching vibration for quantum dot thin films before and after exposure to: a) MeOH and b) ACN, for a duration of 10 min, indicating significant loss of OA from quantum dots upon extended MeOH exposure, whereas minimal change is detected following exposure to ACN. The insets in (a) and (b) show the carbon-to-lead atomic ratio highlighting the effect of MeOH and ACN exposures, respectively. c) Quartz-crystal microbalance (QCM-D) measurements of mass change upon exposure of pristine quantum dots to MeOH and ACN, revealing loss of mass in MeOH films as a result of OA loss. d) QCM-D measurements of the mass change upon drop-casting octane on the quantum-dot films after their exposure to MeOH and ACN for 100 s, revealing the MeOH-treated quantum dots are rendered insoluble. e) Time evolution of the fraction of OA remaining with respect to exposure time to MeOH and ACN. f) Time evolution of the fraction of QDs dissolved in octane as determined from QCM-D measurements, revealing the QDs are rendered insoluble by exposure to MeOH for nearly 90 s.

octane, as suggested by SEM and AFM images (see Figure S3, Supporting Information). The optical properties of the QD films reveal a blue-shift of the quantum confinement peak at ca. 950 nm upon MeOH exposure (see Figure S4, Supporting Information). With time, as MeOH removes OA, the dots come closer thereby reducing the inter-dot spacing from ca. 4.6 nm in pristine films to ca. 4.4 nm after 10 min of MeOH exposure, as demonstrated by grazing incidence small angle X-ray scattering (GISAXS) measurements (see Figure S5, Supporting Information). In addition to the loss of OA, X-ray photoelectron spectroscopy (XPS) measurements reveal a significant loss of the halide (Cl) from the surface of the QDs when exposed to MeOH for 600 s (see Figure S6, Supporting Information). By contrast, the ACN-treated film shows almost no change in terms of OA fraction, solubility, thickness, optical properties, inter-particle spacing, or halide content.

The halide atoms on the surface of QDs are crucial for assuring effective atomic passivation and mitigating the sub-gap trap state density, which strongly influences carrier recombination in QD solar cells. Thus, we speculate that loss of halide atoms when exposing QDs to MeOH may be the main reason for the degradation of photovoltaic performance upon extending the ligand-exchange duration. This effect may not have been discovered earlier, because solar cells fabricated in 10 LbL steps

either with MeOH or ACN yield nearly identical power conversion efficiencies, as will be shown below (e.g., see Figure 5). This is probably because ligand exchange is completed on a sub-second timescale for the low QD film thicknesses involved in the 10 LbL process, irrespective of the solvent choice (Figure S7, Supporting Information), and thus state-of-the-art device fabrication recipes do not require extended exposure to MeOH for longer than 3 seconds. Turning our attention to the loss of halide during ligand exchange, we use XPS to look at the differences in the elemental composition of ligand-exchanged films using MeOH and ACN-based treatments for durations longer than 3 seconds (**Figure 3** and Figure S8, Supporting Information). XPS reveals loss of surface halide (Cl) with extended ligand exchange when MeOH is used as the solvent, evident by the decreasing Cl:Pb atomic ratio. No such loss is observed for the case of ACN-based treatments (Figure 3a). Also shown in Figure 3a are the effects of pure solvents MeOH and ACN, previously discussed, revealing the Cl:Pb ratio is the same regardless of whether MPA is present or not in MeOH. This demonstrates that halide loss can be directly linked to MeOH exposure.

We combine the XPS study detailed above with UPS in order to study the valence bands of the extended ligand-exchanged QD films (Figure 3b). Enhanced near-Fermi level DOS in PbS QDs have been suggested to behave as charge carrier traps which are detrimental to device performance.[18,19] Katsiev et al. recently demonstrated that synchrotron-based UPS can be effectively used to study the near-Fermi level carrier trap states in PbS-QD-based solar cells.[20] We find a higher density of electronic states near the Fermi level for films exchanged using MeOH. This proves that MeOH-induced Cl-loss leading to charge carrier traps is the reason behind device-performance loss and that ACN is gentler even after extended exposure. We also observe a ca. 0.2 eV shift of the valence band edge towards the Fermi level as shown in Figure 3b by the black dashed lines. We suspect this to be the reason for the reduction of the V_{OC} for the MeOH-based 3 LbL device (see Table 1). While the high dipole moment is believed to make ACN gentle on the OA,[14] it is not clear at this time whether this or the aprotic nature of the solvent is to credit for preventing Cl-loss.

We now seek to demonstrate that ACN can be used to perform effective ligand exchange for longer duration on the thicker films, allowing the absorbing layer to be fabricated in fewer steps. As thicker films are believed to require longer ligand-exchange duration to achieve the same level of exchange as in case of thinner films, we have used VASE to monitor the thickness and optical properties of thin (ca. 80 nm) and thick (ca. 180 nm) films as a function of ligand-exchange time (see **Figure 4**). VASE analysis of even thicker films (ca. 250 nm) was complicated by virtue of thin film uniformity and roughness issues, thus we have limited our comparison to films of nearly ca. 180 nm, which after ligand exchange shrink down to ca. 75 nm. Several important conclusions can be drawn from these results. First, for both thin and thick films, ligand-exchange dynamics seem to be independent of the choice of solvent as was suggested above on the basis of QCM-D studies on ligand exchange on thin films. Second, ligand exchange leads to film densification as suggested by the increase in refractive index. This is accompanied by a massive decrease in the inter-dot

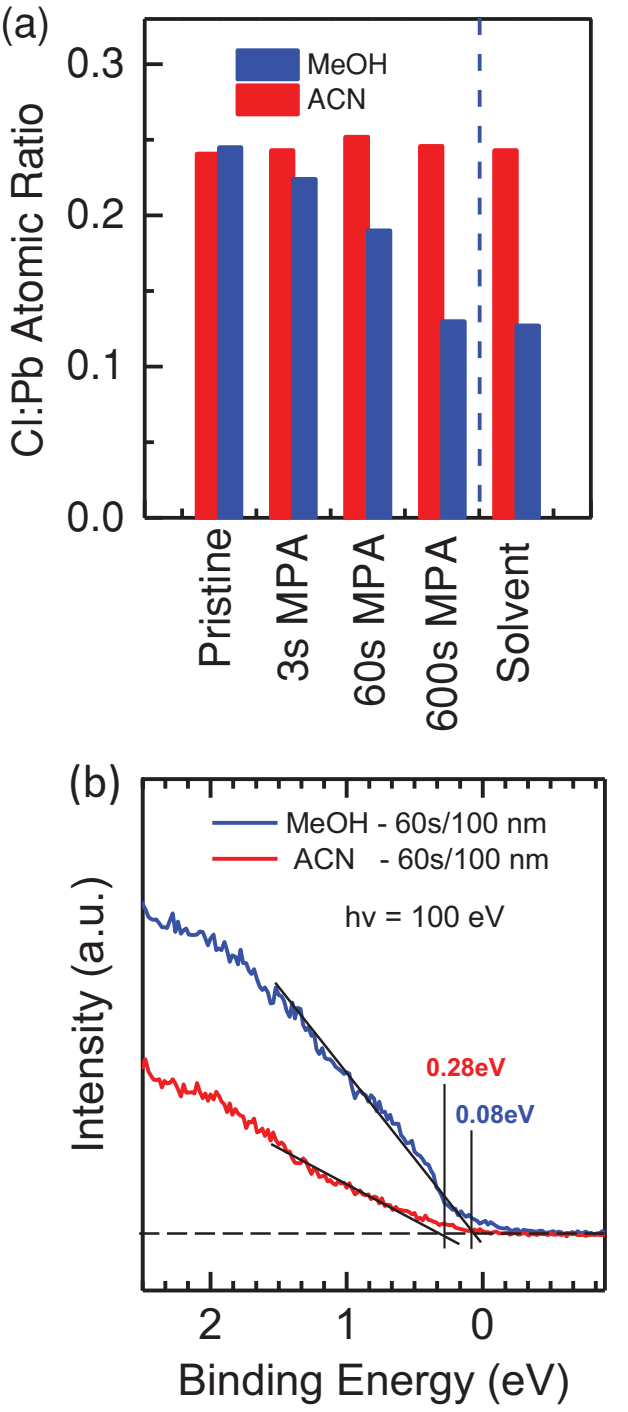

Figure 3. X-ray and ultraviolet photoelectron spectroscopy were used to study the solvent–quantum-dot interactions. a) Evolution of the Cl/Pb atomic ratio with increasing ligand-exchange process duration using MeOH (red bars) and ACN (black bars). Also shown is the case for an extended exposure (600 s) to the respective pure solvent. b) UPS spectra showing an increased near-Fermi density of states for a MeOH-treated thick film as compared to an ACN-treated thick film for the same duration (60 s). The enhancement of sub-gap trap state density in case of MeOH treated devices is believed to affect the device performance. An increase in the VB maxima by ca. 0.2 eV is observed for the MeOH-treated film as compared to the ACN-treated film.

Adv. Mater. **2014**,
DOI: 10.1002/adma.201400577

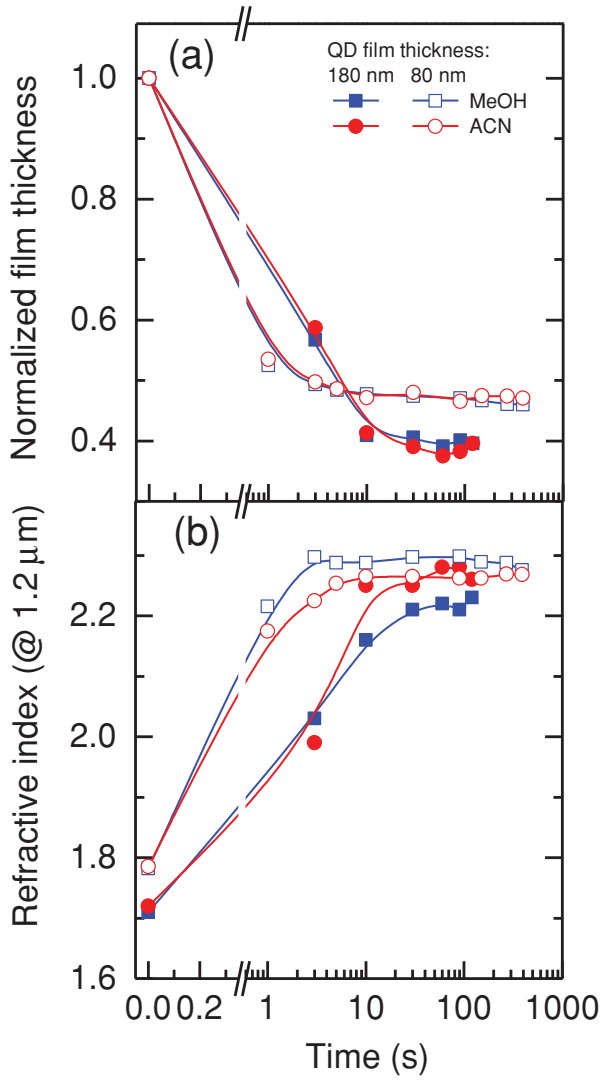

Figure 4. Variable-angle spectroscopic ellipsometry (VASE) data showing a comparison of: a) thickness variation and b) refractive index for extended ligand-exchange times on thin (ca. 80 nm) and thick (ca. 180 nm) films using the solvents ACN and MeOH. The results show that the ligand-exchange process requires more time for thicker films as compared with the sub-second timescale required for ligand exchange in the standard-thickness films. The ligand-exchange kinetics appear to be independent of the solvent used.

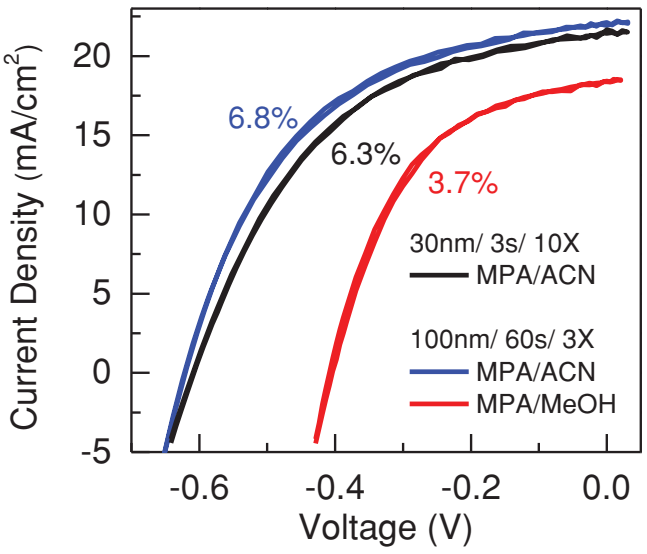

Figure 5. Three-layer devices processed using 60 s ligand exchange in methanol or acetonitrile solvent environments are compared. For comparison, we have included a ten-layer device using 3 s ligand exchange in acetonitrile.

spacing and an expected red-shift in the peak absorption as shown in the supplementary information (see Figure S9, Supporting Information).[21,22] Interestingly, MeOH-based ligand exchange leads to smaller interdot spacing than ACN-based ligand exchange. Third, the thicker films show a slowed ligand exchange nearing completion after ca. 20 s, a duration nearly 6–7 times greater to fully exchange a film only 2.3 times thicker.

We naturally anticipate that thicker films will require even more time to complete the ligand exchange. Our optimization efforts show that a ligand-exchange duration of ca. 60 s is sufficient to complete the ligand exchange of QD films with a exchanged/pristine thickness of ca. 100 nm/ca. 250 nm. The device performance shown in **Figure 5** validates this hypothesis (see **Table 2**). The ACN-based 3 LbL device (black) employing 60 s exchange shows much better performance than the MeOH-based 3 LbL device (red) and closely approaches the performance observed in standard MeOH- and ACN-based 10 LbL devices shown in Figures 1 and 5, along with significant process simplification and consuming ca. 40% less CQD solution than the latter (see Figure S10, Supporting Information). The ACN-based devices behave well despite the fact that interdot spacing is larger than when MeOH-based ligand exchange is used (Figure S9a, Supporting Information). This may be due to the OA washing step just following the ligand exchange and performed using the same solvent. ACN being a poor solvent to OA may not remove all the excess OA from the QD film, resulting in a slightly larger interdot spacing. This, however, does not appear to harm device characteristics.

In summary, we have identified that the ligand-exchange solvent, MeOH, leads to device performance degradation by chemically damaging the surface passivation of CQDs for extended exposures, whereas ACN has been shown to be inoffensive. This is the reason for the CQD solar cells made with MeOH requiring several tedious and wasteful steps as part of the LbL buildup of the absorbing layer. Understanding of solvent interactions with

Table 2. Champion device characteristics for CQD thin films processed according to two different recipes. A solid-state exchange using 3-mercaptopropionic acid (MPA) in methanol versus acetonitrile, for 60 s treatments per 100 nm layer for a total of 3 layers. Device statistics are summarized in Table S1 in the Supporting Information.

	V_{OC} [V]	J_{SC} [mA/cm^2]	FF [%]	PCE [%]
MeOH – 60 s/100 nm	–0.409	18.1	49.6	3.67
ACN – 60s /100 nm	–0.622	21.7	51.4	6.81
ACN – 3 s/30 nm	–0.611	21.2	48.3	6.32

QD films has led to the development of more efficient processing conditions based on use of ACN, which allows us to achieve state-of-the-art performance using only three steps for active layer deposition. This work could shed light on ways to achieve a single-step deposition by other solution processing methods and solid-state ligand exchange, greatly enhancing the opportunity to fabricate solar cells in a scalable manner.

Experimental Section

CQD Synthesis: PbS CQDs were synthesized using a variation on a method described in the literature,[23] employing a previously reported in-synthesis halide treatment. [11]

Device Fabrication: CQD films were prepared on TiO_2 electrodes (50nm of TiO_2 sputtered on fluorine-doped tin oxide (FTO)-coated glass) by multilayer spin-coating of a 100 mg mL^{-1} solution of quantum dots in octane under ambient conditions. The layer thickness was adjusted by depositing at either 750 or 2500 rpm. Each layer was treated with 1% 3-mercaptopropionic acid in either methanol or acetonitrile (v/v), and then rinsed twice with either methanol or acetonitrile while spinning at 2500 rpm. The resultant layer thickness, post-treatment, was 100 or 30 nm for deposition rates of 750 or 2500 rpm, respectively. Top electrodes were deposited by thermal and electron beam evaporation, and consisted of 40 nm of MoO_3, 50 nm of gold and 80 nm of silver. These were deposited at a rate of 0.2 (thermal MoO_3), 0.4 (electron beam Au) and 1 Å/s (thermal Ag), at a pressure of $<1 \times 10^{-6}$ mbar.

J–V Characterization: J–V data was measured using a Keithley 2400 source-meter at ambient temperature, with the device held in a constantly purged nitrogen environment. The solar spectrum at AM1.5 was simulated to within class A specifications (less than 25% spectral mismatch) with a xenon lamp and filters (ScienceTech; measured intensity of 100 mW cm^{-2}). The source intensity was measured with a Melles–Griot broadband power meter through a circular 0.049 cm^2 aperture. The same aperture was used in the J–V measurement; the aperture is slightly smaller than the top electrode to avoid overestimating the photocurrent. The entire photon fluence passing through the aperture was counted as incident on the device for all current analyses. The spectral mismatch of the system was characterized using a calibrated reference solar cell (Newport). The total AM 1.5 spectral mismatch—taking into account the simulator spectrum and the spectral responsivities of the test cell, reference cell, and broadband power meter—was re-measured periodically and found to be ca. 4.4%. This multiplicative factor, M = 0.956, was applied to the current density values of the J–V curve to most closely resemble true AM 1.5 performance. The uncertainty of the current–voltage measurements was estimated to be 7%.

QCM-D measurements: Thin films of CQDs were fabricated by spin-coating 100 µL of CQDs for 15 s at 2500 rpm on SiO_2-coated quartz crystal sensors, thermally oxidized Si wafers and Au-coated glass substrates. The AT-cut quartz crystals (5 MHz resonance frequency) and the Si wafers with 100 nm oxide layer on top were cleaned by ultrasonication separately in acetone, isopropyl alcohol and ethanol followed by a 10 min UV–ozone treatment. Film-coated quartz sensors were loaded into a QCM open module (E4 model, QSense, Biolin Scientific) maintained at 25 °C. Drop-casting measurements were carried out by dropping 150 µL of the process solvents and ligand-exchange solutions on the surface of the coated sensors.

FTIR characterization: FTIR microanalysis was performed on a Nicolet 6700 infrared spectrometer coupled with a Nicolet Continuum Microscope (Thermo Electron Corporation, UK). The spectrometer has a KBr beam splitter and an EverGlo IR source. The microscope has a mercury cadmium telluride (MCT-A) detector refrigerated with liquid nitrogen and a 15× Reflachromat Objective (0.58 N.A.). Reflection mode was used for collecting the FTIR spectra that were recorded with the nominal resolution of 4 cm^{-1} over the range 600–4000 cm^{-1}. 100 nm Au-coated FTO slides were used as substrates.

IR-VASE Analysis: A J.A. Woollam Co., Inc. IR-VASE ellipsometer (500–5000 cm^{-1}) was used to study the fraction of the OA remaining in the thin films upon various solvent and ligand-exchange treatments. The IR-VASE uses a Fourier transform based infrared spectrometer combined with a variable angle ellipsometer incorporating a rotating compensator technology for accurate Ψ and Δ measurements. The spectra were obtained at an incidence angle of 75°. The resulting elliptical beam spot had dimensions 3.9 cm × 0.7 cm. 100 nm Au-coated soda-lime glass slides were used as substrates.

VASE Analysis: An M-2000XI, J. A. Woollam Co., Inc. ellipsometer (400–1700 nm) was used to study the variation in film thickness and optical properties with solvent treatments and ligand exchanges on QD films coated on thermally oxidized Si substrates. The spectra were obtained at incidence angles in the range 45–75° with discrete increments of 5°. The film properties were modelled assuming a B-Spline dispersion relation in the absorption region using the EASE and WVASE32 software packages from J. A. Woollam Co., Inc.

GISAXS: Ex situ GISAXS analysis was carried out at the D-line at the Cornell High Energy Synchrotron Source (CHESS) (Cornell University). A beam with a wavelength of 1.23 Å was obtained from a wide bandpass (1.47%) double-bounce multilayer monochromator. The angle of incidence was varied discretely from 0.15° to 0.50° with respect to the substrate plane.

Morphology Characterization: An Agilent 5400 instrument in tapping mode was used to obtain AFM images. High-resolution SEM images were acquired using an FEI Nova Nano630 scanning electron microscope equipped with a field-emission electron source and through-lens electron detectors at an electron beam voltage of 5 kV.

Cross-Sectional TEM: Cross-sectional TEM sample preparation was done using a focused ion beam (FIB) (FEI Helios 400s) with the lift-out method. The lamella was prepared by Ga-ion milling with beam conditions 30 kV and 9 nA. It was then transferred to copper TEM grid using the nanomanipulator (Omniprobe). The lamella was thinned down to a thickness of 50 nm and cleaned with ion-beam conditions of 2 kV and 4.7 pA. HRTEM (FEI, Titan Super Twin) analysis was done at 300 kV.

Photoelectron Spectroscopy Measurements: XPS studies were carried out in a UHV Omicron chamber equipped with a SPHERA U7 hemispherical energy analyzer, using X-ray photons with an incident kinetic energy of 1486.6 eV from a monochromated Al K_α X-ray source with a total energy resolution of 0.1 eV. The studies were carried out at room temperature. The PES spectra were obtained from the VLS-PGM beamline at the Canadian Light Source, Inc., having a Scienta SES100 hemispherical energy analyzer and an energy resolution of 0.05 eV. The spectra were obtained at normal emission and room temperature.

Supporting Information

Supporting Information is available from the Wiley Online Library or from the author.

Acknowledgements

The authors acknowledge the help of Dr. Omar El Tall of the Analytical Core Laboratory, KAUST for his assistance with the FT-IR measurements, Dr. Issam Gereige of the Solar and Photovoltaic Engineering Research Center, KAUST for his assistance with IR-VASE measurements, as well as Dr. Ruipeng Li and Dr. Detlef-M. Smilgies for their assistance with GISAXS measurements at CHESS. This publication is based in part on work supported by Award KUS-11–009–21, made by King Abdullah University of Science and Technology (KAUST), by the Ontario Research Fund Research Excellence Program, and by the Natural Sciences and Engineering Research Council (NSERC) of Canada. The authors thank Angstrom Engineering and Innovative Technology for useful discussions regarding material deposition methods and control of the glovebox environment, respectively. UPS measurements described in this

DOI: 10.1002/adma.201400577

paper were performed at the Canadian Light Source, which is funded by the Canada Foundation for Innovation, the Natural Sciences and Engineering Research Council of Canada, the National Research Council Canada, the Canadian Institutes of Health Research, the Government of Saskatchewan, Western Economic Diversification Canada, and the University of Saskatchewan. The authors acknowledge the use of the D1 beam line at the Cornell High Energy Synchrotron Source supported by the National Science Foundation (NSF DMR-0225180) and NIH-NIGMS.

Received: February 5, 2014
Revised: April 14, 2014
Published online:

[1] D. Yu, C. Wang, P. Guyot-Sionnest, *Science* **2003**, *300*, 1277–1280.
[2] C. J. Stolle, T. B. Harvey, B. A. Korgel, *Curr. Opin. Chem. Eng.* **2013**, *2*, 160–167.
[3] H. Fu, S. W. Tsang, *Nanoscale* **2012**, *4*, 2187–2201.
[4] H. W. Hillhouse, M. C. Beard, *Curr. Opin. Colloid Interface Sci.* **2009**, *14*, 245–259.
[5] D. V. Talapin, C. B. Murray, *Science* **2005**, *310*, 86–89.
[6] J. M. Luther, M. Law, Q. Song, C. L. Perkins, M. C. Beard, A. Nozik, *ACS Nano* **2008**, *2*, 271–280.
[7] S. A. McDonald, G. Konstantatos, S. Zhang, P. W. Cyr, E. J. Klem, L. Levina, E. H. Sargent, *Nat. Mater.* **2005**, *4*, 138–142.
[8] P. Maraghechi, A. J. Labelle, A. R. Kirmani, X. Lan, M. M. Adachi, S. M. Thon, S. Hoogland, A. Lee, Z. Ning, A. Fisher, A. Amassian, E. H. Sargent, *ACS Nano* **2013**, *7*, 6111–6116.
[9] G. H. Carey, K. W. Chou, B. Yan, A. R. Kirmani, A. Amassian, E. H. Sargent, *MRS Commun.* **2013**, *3*, 83–90.
[10] J. Tang, K. W. Kemp, S. Hoogland, K. S. Jeong, H. Liu, L. Levina, M. Furukawa, X. Wang, R. Debnath, D. Cha, K. W. Chou, A. Fisher, A. Amassian, J. B. Asbury, E. H. Sargent, *Nat. Mater.* **2011**, *10*, 765–771.
[11] A. H. Ip, S. M. Thon, S. Hoogland, O. Vozznyy, D. Zhitomirski, R. Debnath, L. Levina, L. Rollny, G. H. Carey, A. Fisher, K. W. Kemp, I. J. Kramer, Z. Ning, A. J. Labelle, K. W. Chou, A. Amassian, E. H. Sargent, *Nat. Nanotechnol.* **2012**, *7*, 577–582.
[12] J. Jean, S. Chang, P. R. Brown, J. J. Cheng, P. H. Rekemeyer, M. G. Bawendi, S. Gradecak, V. Bulovic, *Adv. Mater.* **2013**, *25*, 2790–2796.
[13] A. Fischer, L. Rollny, J. Pan, G. H. Carey, S. M. Thon, S. Hoogland, O. Vozznyy, D. Zhitomirski, J. Y. Kim, O. M. Bakr, E. H. Sargent, *Adv. Mater.* **2013**, *25*, p. 5742–5749.
[14] C. W. Hoerr, H. J. Harwood, *J. Phys. Chem.* **1952**, *56*, 1068–1073.
[15] H. Ullah Khan, R. Li, Y. Ren, L. Chen, M. M. Payne, U. S. Bhansali, D.-M. Smilgies, J. E. Anthony, A. Amassian, *ACS Appl. Mater. Interfaces* **2013**, *5*, 2325–2330.
[16] H. A. Harms, N. Tetreault, V. Gusak, B. Kasemo, M. Gratzel, *Phys. Chem. Chem. Phys.* **2012**, *14*, 9037–9040.
[17] R. Li, H. Ullah Khan, M. M. Payne, D.-M. Smilgies, J. E. Anthony, A. Amassian, *Adv. Funct. Mater.* **2013**, *23*, 291–297.
[18] I. J. Kramer, E. H. Sargent, *ACS Nano* **2011**, *5*, 8506–8514.
[19] E. H. Sargent, *Nat. Photonics* **2009**, *3*, 325–331.
[20] K. Katsiev, A. H. Ip, A. Fisher, I. Tanabe, X. Zhang, A. R. Kirmani, O. Vozznyy, L. R. Rollny, K. W. Chou, S. M. Thon, G. H. Carey, X. Cui, A. Amassian, P. Dowben, E. H. Sargent, O. M. Bakr, *Adv. Mater.* **2014***26*, 937–942.
[21] E. Zillner, S. Fengler, P. Niyamakom, F. Rausher, K. Kohler, T. Dittrich, *J. Phys. Chem. C* **2012**, *116*, 16747–16754.
[22] A. R. Smith, W. Yoon, W. B. Heuer, S. I. M. Baril, J. E. Boercker, J. G. Tischler, E. E. Foos, *J. Phys. Chem. C* **2012**, *116*, 6031–6037.
[23] M. A. Hines, G. D. Scholes, *Adv. Mater.* **2003**, *15*, 1844–1849.